

Research Paper

Ion drugs for precise orthotopic tumor management by *in situ* the generation of toxic ion and drug pools

Yushuo Feng, Ruixue Qin, Lihua Xu, Xiaoqian Ma, Dandan Ding, Shi Li, Lei Chen, Yaqing Liu, Wenjing Sun, Hongmin Chen[✉]

State Key Laboratory of Molecular Vaccinology and Molecular Diagnostics and Center for Molecular Imaging and Translational Medicine, School of Public Health, Xiamen University, Xiamen 361102, China.

✉ Corresponding author: E-mail: hchen@xmu.edu.cn.

© The author(s). This is an open access article distributed under the terms of the Creative Commons Attribution License (<https://creativecommons.org/licenses/by/4.0/>). See <http://ivyspring.com/terms> for full terms and conditions.

Received: 2021.08.25; Accepted: 2021.11.21; Published: 2022.01.01

Abstract

Background: Asymmetric intracellular and extracellular ionic gradients are critical to the survivability of mammalian cells. Given the importance of manganese (Mn^{2+}), calcium (Ca^{2+}), and bicarbonate (HCO_3^-) ions, any alteration of the ion-content balance could induce a series of cellular responses. HCO_3^- plays an indispensable role for Mn-mediated Fenton-like reaction, but this is difficult to achieve because bicarbonates are tightly regulated by live cells, and are limited in anticancer efficacy.

Methods: A responsive and biodegradable biomineral, Mn-doped calcium carbonate integrated with dexamethasone phosphate (DEX) ($Mn:CaCO_3$ -DEX), was reported to enable synergistic amplification of tumor oxidative stress, reduce inflammation, and induce Ca-overload cell apoptosis by elevating the intracellular and extracellular ionic gradients.

Results: Under the acidic environment in tumor region, the ions (Mn^{2+} , CO_3^{2-} , Ca^{2+}) were released by the degradation of $Mn:CaCO_3$ -DEX and then escalated oxidative stresses by triggering a HCO_3^- -indispensable Mn-based Fenton-like reaction and breaking Ca^{2+} ion homeostasis to cause oxidative stress in cells and calcification. The released anti-inflammatory and antitumor drug, DEX, could alleviate the inflammatory environment. The investigations *in vitro* and *in vivo* demonstrated that the synergistic oncotherapy could effectively inhibit the growth of subcutaneous tumors and orthotopic liver tumors. Notably, normal cells showed greater tolerance of the synergistic influences.

Conclusion: As an ion drug, $Mn:CaCO_3$ -DEX is an excellent potential diagnostic agent for precise orthotopic tumor management by the generation *in situ* of toxic ion and drug pools in the environment of tumor region, with synergistic effects of enhanced chemodynamic therapy, calcification, and anti-inflammation effects.

Key words: Tumor acidic environment, Internal ions overload, Chemodynamic therapy, Calcification, Anti-inflammatory

Introduction

Tumors are described as “a wound that doesn’t heal”, and inflammation is a hallmark of cancer [1-5]. In the environment of tumor region, inflammatory cells and secreted inflammatory factors are important components that can release chemicals including reaction oxygen species (ROS). They added some complexity to the tumor environment [6-9]. Dexamethasone phosphate (DEX), a glucocorticoid and commercial drug using for inflammatory diseases [10-11], has been increasingly used in malignant

tumor treatment in recent years [12-16]. It can result in tumor inhibition and tumor environment modulation, also reduce hematopoietic toxicity and immune response of chemotherapeutic agents [17].

Calcium (Ca^{2+}) is a ubiquitous but important modulator of cellular physiology and is associated with diverse physiological events [18-22]. The intracellular Ca^{2+} overload was recognized as important to increase cell apoptosis factors, and may induce mitochondrial dysfunction [23-28]. Therefore,

destruction of the intracellular Ca^{2+} homeostasis via calcium overload, is a potential method for antitumor therapy. Calcium channels played a very important role in the homeostasis of intracellular Ca^{2+} ions by restricting the movement of calcium ions into cells [29-30]. This is limited to inducing influx of Ca^{2+} into cells and facilitating release of Ca^{2+} due to the protective mechanism of cells via Ca^{2+} excretion [31-32]. Calcium carbonate (CaCO_3) is a calcium-containing nanostructures and excellent pH responsive material; it is a good choice for biological applications [33-37].

Chemodynamic therapy (CDT) which depends on neither O_2 nor external light sources and could produce highly deleterious ROS via the reaction of metal ions (Fe^{2+} , Cu^+ and Mn^{2+}) and H_2O_2 [38-44]. The generation of toxic hydroxyl radicals ($\cdot\text{OH}$) causes oxidative damages to lipids molecules with many vital biological functions and dysfunction of mitochondrial to activate cell apoptosis [45-51]. Mn ions are essential human dietary elements that have been the focus of imaging-guided CDT agents [52-55]. In Mn^{2+} -mediated CDT, bicarbonates (HCO_3^-) play a decisive role, versus Fe^{2+} -mediated Fenton reaction. Although the physiological buffers could provide few certain amounts of HCO_3^- to support Mn^{2+} -mediated Fenton-like reaction, they are limited to the inhibition of tumor growth because bicarbonates are tightly regulated by live cells [56-58]. Thus, the self-supplied *in situ* HCO_3^- and Mn^{2+} pools could overcome the challenge [59].

Herein, $\text{Mn}:\text{CaCO}_3\text{-DEX}$ biomineral was synthesized according to a gas diffusion procedure to enable synergistic amplification of tumor oxidative stress, reduction of inflammation, and induction of Ca-overload cell apoptosis (Scheme 1). The CaCO_3 matrix was recognized as an excellent pH-responsive and biodegradable biominerals. The $\text{Mn}:\text{CaCO}_3\text{-DEX}$ reacted with the acidic environment in tumor region and released metal ions (Mn^{2+} and Ca^{2+}), HCO_3^- , and DEX. The calcium-overload resulted in oxidative stress. The generated HCO_3^- amplified Mn^{2+} -mediated Fenton-like peroxidation reactions to generate toxic $\cdot\text{OH}$, and also regulated the intracellular pH to manage tumor growth. The released DEX drugs relieved inflammation and modulated the tumor environment to provide additional tumor inhibitory effects [60]. Significantly, the released Mn^{2+} pools from $\text{Mn}:\text{CaCO}_3\text{-DEX}$ can be used for ultra-sensitive magnetic resonance (MR) imaging to guide this ion drug for precise tumor management. The therapeutic profile of $\text{Mn}:\text{CaCO}_3\text{-DEX}$ was systematically investigated on subcutaneous tumor models and orthotopic liver tumor models and showed efficient synergistic tumor therapy. These results

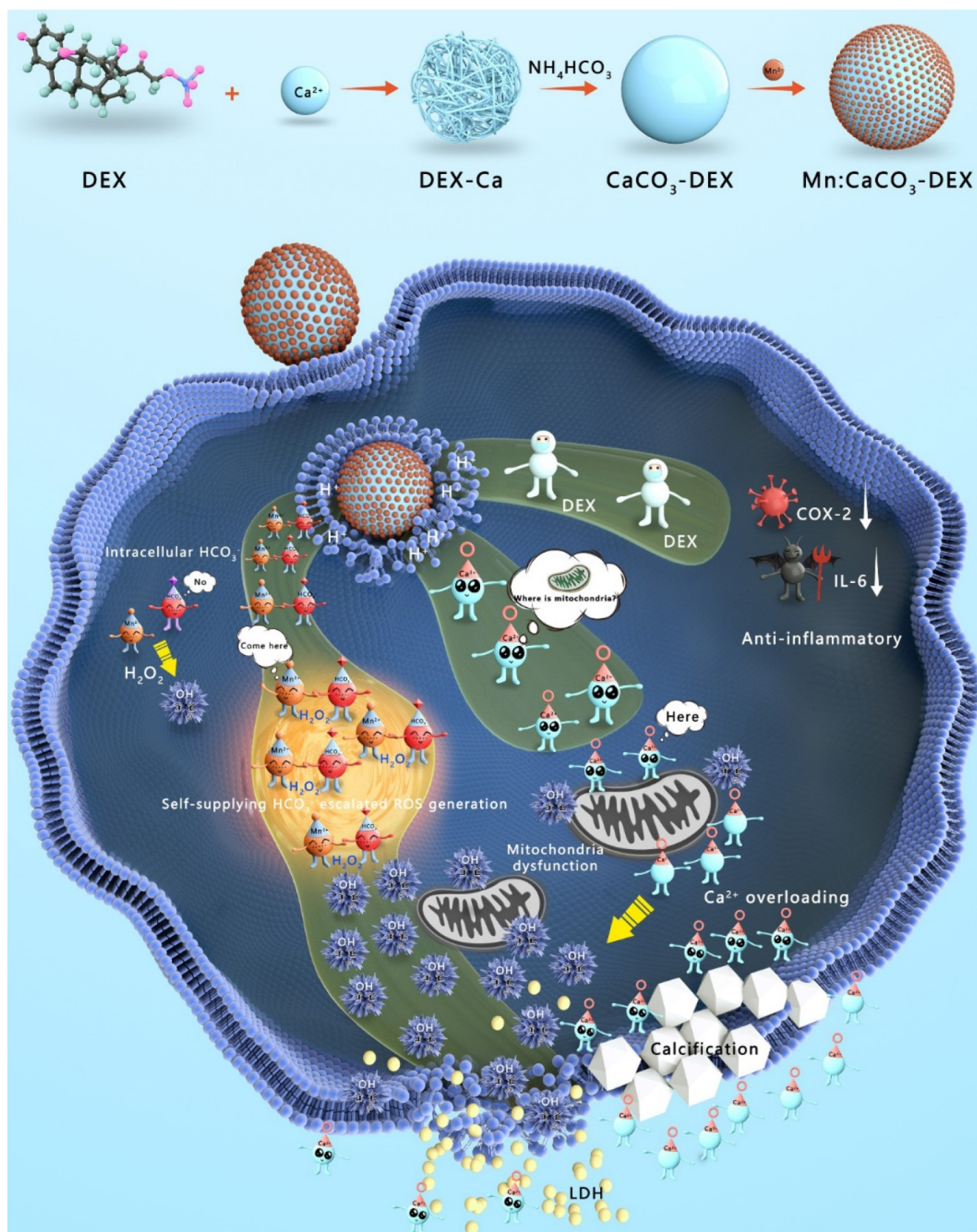
demonstrated that $\text{Mn}:\text{CaCO}_3\text{-DEX}$ offers the synergistic effects of enhanced CDT, calcification, and anti-inflammation effects.

Results and Discussion

Dexamethasone sodium phosphate (DEX) is a synthetic glucocorticoid and commercial drug used for inflammatory diseases and antitumor, containing a phosphate group [61]. Metal ions (Ca^{2+} , Mn^{2+}) coordinated with phosphate groups of DEX, and formed nanofiber network of Ca-DEX with filamentous structures (Figure S1). Gas (CO_2 and NH_3) were diffused into the solution of Ca-DEX for the formation of controllable CaCO_3 particles in an enclosed environment. By simply modulating the feeding ratios of DEX to Ca^{2+} , the reaction times in the NH_4HCO_3 environment, the morphologies and drug load capacities could be precisely tuned (Figure S2). Finally, we chose a formula to prepare calcium carbonate-dexamethasone sodium phosphate ($\text{CaCO}_3\text{-DEX}$) with a feeding ratio of DEX to $\text{CaCl}_2 \cdot 2\text{H}_2\text{O}$ of 6/50, and a reaction time of 8 h.

An average diameter of 150.4 ± 20.2 nm of $\text{CaCO}_3\text{-DEX}$ were achieved (Figure 1A). The P, F, and Na atoms in the scanning transmission electron microscopy (STEM), and the typical characterized peak (242 nm) proved the existence of DEX in the $\text{CaCO}_3\text{-DEX}$ nanoparticles (Figure 1A; Figure S3). The Mn^{2+} ions were coordinated with free phosphate groups of $\text{CaCO}_3\text{-DEX}$ to form $\text{Mn}:\text{CaCO}_3\text{-DEX}$ (Figure 1B), and there are almost no changes in morphology. The STEM and EDS analyses confirmed that the isolated manganese atoms were anchored on the matrix of $\text{CaCO}_3\text{-DEX}$ (Figure 1C; Figure S4). The hydrodynamic size and zeta potential of the nanomaterial proved that PAH was successfully modified to improve water solubility (Figure S5). $\text{Mn}:\text{CaCO}_3\text{-DEX}$ was dispersed well in water, PBS (pH 7.4), fetal bovine serum (FBS) and cell culture medium (DMEM). It had kept long-term stability (Figure S6). To further verify the stability of Mn^{2+} , we also verified the release of Mn^{2+} in DMEM. As shown in Figure S7, the release of Mn^{2+} in DMEM was lower than 15%.

The simulated healthy body internal environment and tumor environment (i.e., neutral (pH=7.4), and acidic environment (pH=6.5 pH=6.5 with 1 mM H_2O_2 , and pH=4.0) revealed that the Mn^{2+} , Ca^{2+} , CO_2 bubbles and DEX drugs were released after stimulation (this work monitored the MR signals of Mn^{2+} (Figure 1D), Ca^{2+} and Mn^{2+} concentrations (ICP-OES, Figure S8A, B), US imaging signals of CO_2 (Figure 1F), and the absorbance of DEX (Figure S7C). The morphology and structure changes were evaluated by TEM, confirming the TME-stimulative biodegradation and release process (Figure 1E).



Scheme 1. Synthesis and Functions of Mn:CaCO₃-DEX in the environment of tumor region. The Mn:CaCO₃-DEX reacted with the acidic environment in tumor region and released metal ions (Mn²⁺ and Ca²⁺), HCO₃⁻, and DEX. The calcium-overload resulted in oxidative stress. The generated HCO₃⁻ amplified Mn²⁺ Fenton-like peroxidation reactions to generate toxic ·OH, and also regulated the intracellular pH to manage tumor growth. The released DEX drugs relieved inflammation and modulated the tumor environment to provide additional tumor inhibitory effects. The therapeutic profile of Mn:CaCO₃-DEX on subcutaneous tumor models and orthotopic liver tumor models and showed efficient synergistic tumor therapy.

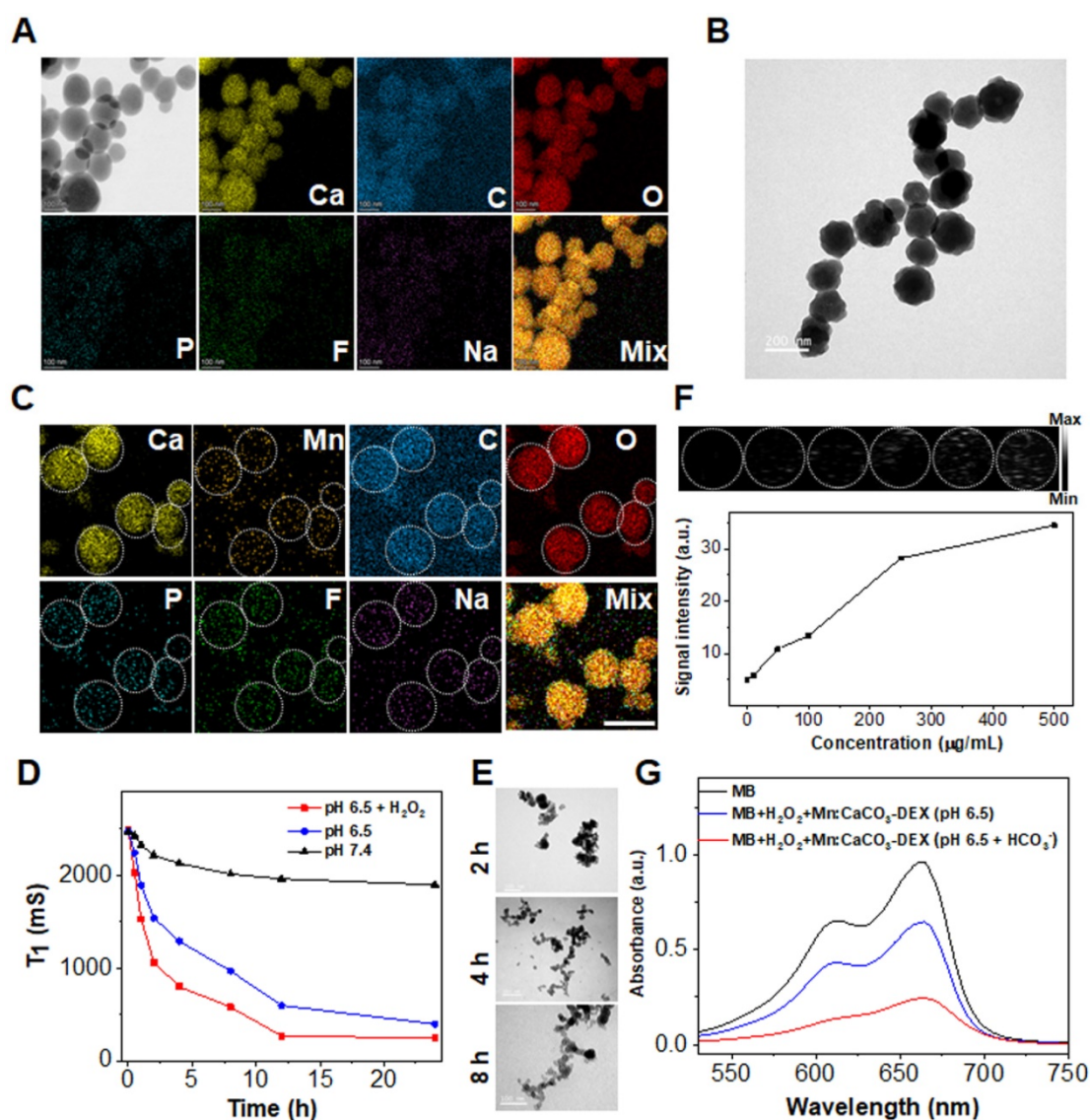


Figure 1. Preparation and characterization of Mn:CaCO₃-DEX. (A) Scanning transmission electron microscope (STEM) images and corresponding element mapping of CaCO₃-DEX (scale bar: 100 nm). (B) TEM image of Mn:CaCO₃-DEX (scale bar: 200 nm). (C) STEM images and corresponding element mapping of Mn:CaCO₃-DEX (scale bar: 100 nm). (D) The Mn release behaviors from Mn:CaCO₃-DEX in different solutions. (E) TEM images of Mn:CaCO₃-DEX after incubation with different time in acidic environment (pH 6.5 + H₂O₂) (scale bar: 100 nm). (F) Ultrasound images and signal intensity of the generation of CO₂ in acidic environment (pH 6.5 + H₂O₂). (G) MB degradation by *in situ* self-supplying HCO₃⁻-enhanced Mn-mediated Fenton-like reaction.

The released *in situ* HCO₃⁻ is indispensable to accelerate the Fenton-like reaction between Mn²⁺ and intracellular H₂O₂ to produce hydroxyl radical (·OH) [62]. As revealed in Figure 1G, the absorbance of MB decreased dramatically by 33.3% (blue line) after the incubation of Mn:CaCO₃-DEX plus H₂O₂. Notably, the absorbance of MB decreased by 75.0% (red line) in the presence of HCO₃⁻ (the highest theoretical concentration that was released from the Mn:CaCO₃ matrix). This proved that the released *in situ* HCO₃⁻ in the acidic environment of tumor region could escalate an accelerated Fenton-like reaction.

The concentration of free Ca²⁺ in the cytosol is generally less than 0.002 mM; it is a thousand or more times lower than that in the blood [19]. This stimulation released Ca²⁺, which instantly increased

the local Ca²⁺ levels in some cellular compartments with acidic environments. The evaluation on U87MG cells, a human glioma cell line, showed that the cellular Ca²⁺ signals (indicated by Ca²⁺ fluorescence probe, Fluo-4 AM) remained relatively stable when the U87MG cells were incubated with PBS, Mn²⁺ (10 μg/mL), and Ca²⁺ (25 μg/mL) (Figure 2A). In contrast, the cellular Ca²⁺ signals increased sharply when the cells were incubated with nanoparticles (CaCO₃-DEX and Mn:CaCO₃-DEX) because the nanoparticles could be endocytosed and not limited to the calcium ion channels (Figure 2A). Then, we also studied the distribution performance of Mn:CaCO₃-DEX after they entered the cells through lysosome colocalization (Figure S9), the accumulation in mitochondrial (Figure S10) and thin-section cell TEM

images (Figure S11). The co-localization of Mn:CaCO₃-DEX and lysosomes indicated that nanoparticles can be located in lysosomes and mitochondrial. The Pearson's correlation coefficient of Ca²⁺ and lysosomes could reach to 0.65 ± 0.015 via ImageJ analysis. To confirm the uptake and disassociation of Mn:CaCO₃-DEX, bio-TEM imaging of cell slices were performed. After 24 h incubation, Mn:CaCO₃-DEX was observed in the lysosome (yellow arrow) and mitochondria (red arrow), and apparent degradations were observed (Figure S11). The abnormal boost growth of intracellular Ca²⁺ may lead to calcium overload and deactivate the calcium pump (Ca²⁺-ATP) (Figure S12), which may be accompanied by formation of calcification. Damage of the calcium outflow pathway could causes persistent

calcium overload (Figure S12). The calcification of the cells was induced rapidly with vast accumulation of localized calcium ions. This was detected by Alizarin Red S staining (Figure 2B) [63]. The formation of calcification nodules was observed significantly in treatment groups and the calcified area increased at higher concentrations of Mn:CaCO₃-DEX. The obvious positive staining results proved that the released Ca²⁺ induced calcification profile.

The Trojan-horse strategy delivered ions into cells and disrupted the ion homeostasis [64-66]. It affects cell functions, such as oxidative stress as well as mitochondrial dysfunction [67-69]. To evaluate the oxidative stress response in cells, 2',7'-dichloro-fluorescein diacetate (DCFH-DA; ROS fluorescence probe), was used to investigate the ·OH generation.

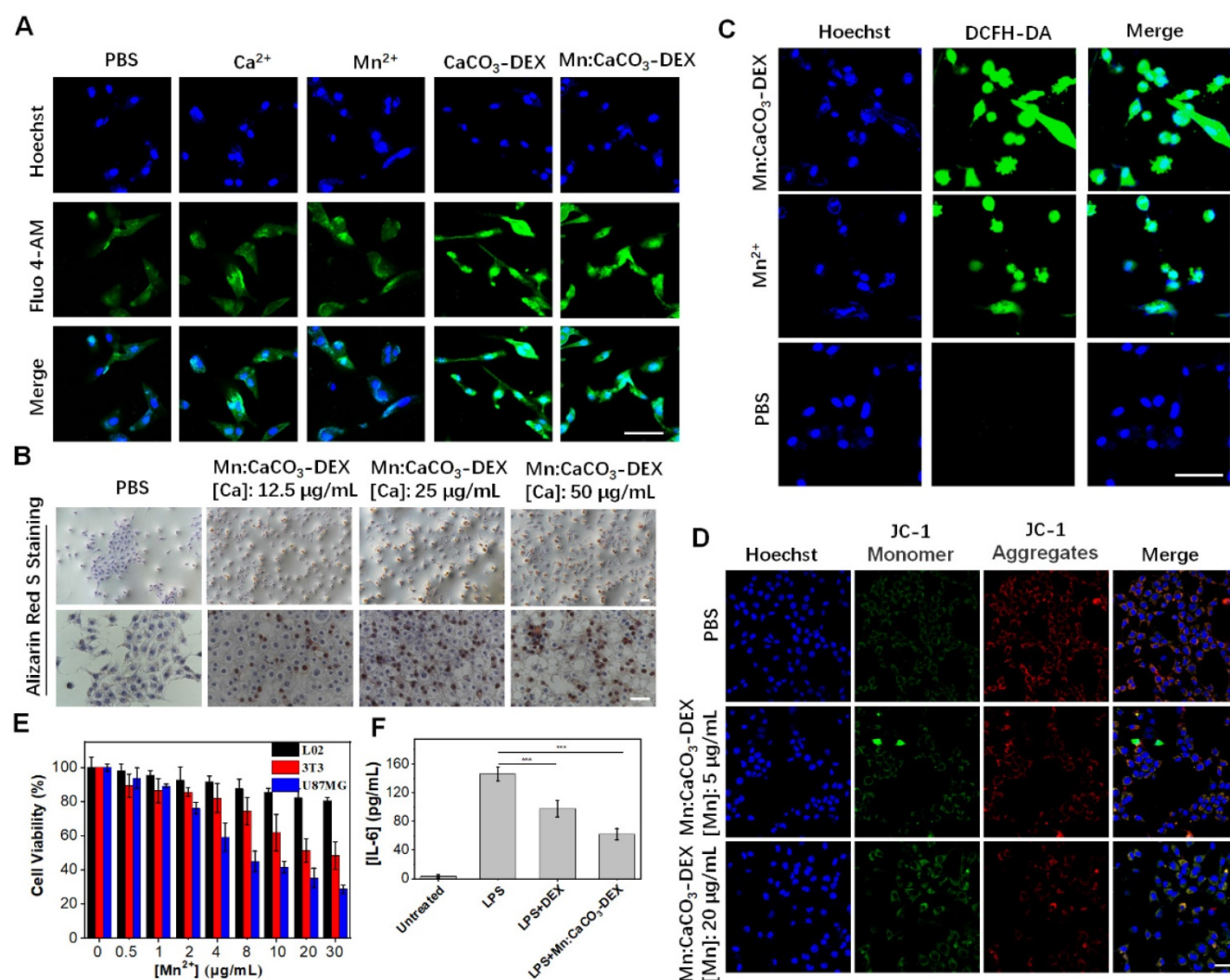


Figure 2. *In vitro* oxidative stress reaction and cell therapeutic effects. **(A)** CLSM evaluation of cell uptake on U87MG cells incubated with PBS, Ca²⁺, Mn²⁺, CaCO₃-DEX and Mn:CaCO₃-DEX. The blue and green fluorescence indicate cell nucleus and an intracellular Ca²⁺ indicator, Fluo 4-AM, respectively (scale bar, 30 µm). **(B)** Identification of the formation of calcified nodules in U87MG cells with Alizarin Red S staining which show the calcified areas in red (scale bar, 100 µm). **(C)** Intracellular ·OH generation incubation with PBS, Mn²⁺ and Mn:CaCO₃-DEX detected by DCFH-DA probe. The blue and green fluorescence indicate cell nucleus and DCFH-DA, respectively (scale bar, 30 µm). **(D)** CLSM observation on the changes in the mitochondrial membrane potential of U87MG cells after incubation with different concentration of Mn:CaCO₃-DEX. The blue, red, and green colors indicate cell nucleus, and JC-1 J-aggregates and monomer, respectively (scale bar, 50 µm). **(E)** Cell viabilities of U87MG cells, L02 cells and 3T3 cells incubated with different concentration of Mn:CaCO₃-DEX. **(F)** Secretion levels of pro-inflammatory cytokines (IL-6) changes in lipopolysaccharide- (LPS)-stimulated Raw264.7 cells after different treatment (***p < 0.001).

Incubation of U87MG cells with Mn:CaCO₃-DEX or Mn²⁺ free both induced significant fluorescent signal enhancement (Figures 2C, S13), proving the generation of intracellular ROS. Also, the fluorescence in U87MG cells incubated with Mn:CaCO₃-DEX was much higher than that of the cells incubated with Mn²⁺ free at the same Mn concentration ([Mn]: 20 µg/mL). The rapid and abundant production of ROS could disrupt the original homeostasis state, which gave Mn:CaCO₃-DEX the ability to oxidize biological molecules, leading to irreversible cell necrosis and apoptosis [45]. The peroxidation of lipids (refers to the oxidative degradation of lipids) was elucidated via BODIPY-C11 (Figure S14A). Higher concentrations of Mn:CaCO₃-DEX induced stronger fluorescence signals, and the average signal intensities increased by 7.4% (26.7 ± 0.4 of PBS VS 34.2 ± 5.5 of 5 µg/mL Mn) and 15.7% (42.5 ± 7.3 of 20 µg/mL Mn), respectively (Figure S14B). With the increasing of concentrations, the oxidized ratio could reach 98.5% (Figure S15).

The mitochondrial is participated in the apoptosis and death process of cells. This is also one of the major storage sites of Ca²⁺ in cells [70]. The prolonged and high intracellular external ions levels would lead to mitochondrial dysfunction and then cell death. The mitochondrial membrane potential (MMP) plays a key role in the mitochondrial homeostasis, and a drop of MMP is a significant indicator of cell apoptosis, cell death and other pathologies. The 5,5',6,6'-tetrachloro-1,1',3,3'-tetraethylbenzimidazolyl-carbocyanine iodide (JC-1) assay kit was selected as a ratiometric probe to evaluate the MMP ($\Delta\Psi_m$) change, of which the red fluorescence shifted to green fluorescence after cell apoptosis. Compared with untreated cells, the red fluorescence decreased, but the green fluorescence increased after the cells were incubated with Mn:CaCO₃-DEX (Figure 2D). ImageJ analysis showed much lower red-to-green ratios, indicating that the disturbed mitochondrial membrane potential could lead to cell damage (Figure S16). To verify the reason of mitochondrial damage, we also obtained the changes of JC-1 fluorescence signal after incubation with CaCO₃-DEX. The decrease of red fluorescence indicated that the calcium overload could also induced mitochondrial damage (Figure S17).

Chronic inflammation plays an important role in the promotion of tumor proliferation [3]. Macrophages could promote tumor growth and inflammation [24]. DEX is a clinical anti-inflammatory agent and was evaluated for its anti-inflammatory effect via incubation of Raw264.7 with lipopolysaccharide (LPS) (100 ng/mL) to induce the pro-inflammatory cytokines [71]. Significantly, Mn:CaCO₃-DEX incubation induced a 2.4-fold

decrease in inflammatory cytokine (IL-6) levels, which is higher than that of DEX treatment (1.5-fold) (Figure 2F).

After proving that the components are released and are destroyed, the cell therapeutic effects of Mn:CaCO₃-DEX were studied by the standard methyl thiazolyl tetrazolium (MTT) cell viability assay. Satisfactorily, the Mn:CaCO₃-DEX killed human tumor cells and showed negligible cytotoxicity on normal cells (human L02 hepatocytes and mouse embryonic 3T3 fibroblasts) (Figure 2E). The half maximal inhibitory concentration (IC₅₀) value was estimated as 3.4 µg Mn/mL, which was far lower than 3T3 cells (20.4 µg/mL) and L02 cells (no IC₅₀ value in the concentration ranges). To level the combination, a combination index (CI) was calculated to assess the synergistic effects (CI < 1: synergism, CI > 1: antagonism, CI = 1: additive effect). In our study, the CI value was calculated to be 0.8, which indicated good combination of CDT and calcification effects. The results were further proved via live/dead (calcein-AM/propidium iodide (PI)) co-staining assays (Figure S18). The obvious red fluorescence signal indicated the Mn:CaCO₃-DEX significantly inhibited cell proliferation. Lactate dehydrogenase (LDH) is an enzyme contained in the cytoplasm of living cells. It cannot penetrate the cell membrane under normal circumstances. However, after membrane permeability changes, LDH can be released into the medium, when target cells are attacked and damaged. Thus, the cytotoxicity was also estimated by comparing with positive controls. Significant LDH release was achieved, indicating that the function and structure of the cell membrane was destroyed (Figure S19). All of these results demonstrated that Mn:CaCO₃-DEX could be a potential tumor-targeting chemical drug for cancer management, via HCO₃⁻-indispensable Mn-mediated CDT, calcification and anti-inflammatory actions modulate the tumor environment and induce cell death.

To further explore the important role of pH-responsive release, we validated cell viability and the generation of ·OH after incubated with different buffer solutions. While incubation with free Ca²⁺ alone or with 1 mM H₂O₂, there was no significant cytotoxicity (Figure S20A). However, Mn²⁺ remarkably increased the cytotoxicity to tumor cells with the addition of H₂O₂ (1 mM) (Figure S20B). The cell survival rates reduced with stronger acidic environments (Figure S21A). We predicted that the stronger acidity of the incubation solution increased the released ions, resulting in more cell death. To prove this, we incubated cells with different concentrations of Mn²⁺, Ca²⁺, DEX and HCO₃⁻

(according to the maximum release of Mn:CaCO₃-DEX in different acidic environments) to verify the generation of ·OH and induced cytotoxicity. Similar cell survivals (Figure S21B) and significantly increased fluorescence (Figure S22) proved that acidic-responsive drugs and ions release induced the cell death.

The 3D multicellular tumor spheroids (MTSs) were prepared to evaluate the penetration, distribution and therapeutic effect, which have major roles in tumor therapy research by virtue of their unique advantage of simulating the environment in tumor region. The penetration depth and fluorescence intensity increased obviously after incubating under

acidic environment (pH 6.5) compared with the neutral environment (pH 7.4) (Figure S23), indicating that the acid decomposition capacity may facilitate their intercellular transportation. Furthermore, after 3 days of treatment, the growth of 3D MTSs were effectively inhibited (Figure S24). The 3D MTSs experiments provided a reference for the better prediction of their permeability and therapeutic effect in a solid tumor environment.

The evaluation of the pharmacokinetics of Mn:CaCO₃-DEX showed that the plasma terminal half-life of Mn:CaCO₃-DEX was estimated to be 3.3 h (Figure 3A). The biodistribution of Mn:CaCO₃-DEX in major organs and tumors was evaluated using

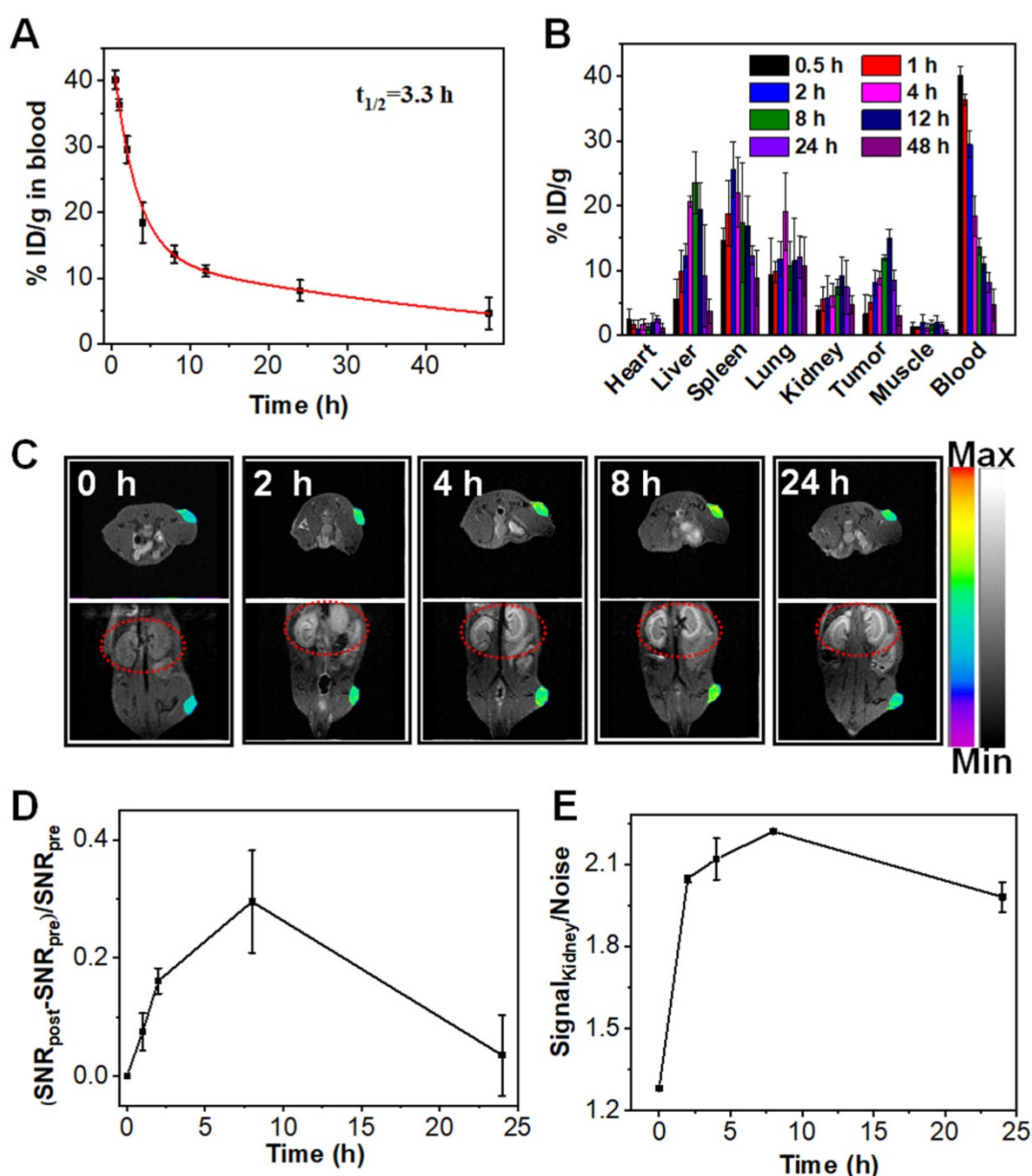


Figure 3. *In vivo* the pharmacokinetic and biodistribution evaluation of Mn:CaCO₃-DEX. **(A)** Blood circulation of Mn:CaCO₃-DEX after intravenous injection. **(B)** Biodistribution of Mn (% injected dose (ID) Mn per gram of tissues) in main tissues and tumors after intravenous administration of Mn:CaCO₃-DEX. **(C)** The T₁-weighted MR images taken at different time points. **(D)** Quantification of the MR signals change in tumors within 24 h based on region of interest (ROI) analysis on images from panel (C). **(E)** Quantification of the MR signals change in kidney within 24 h based on ROI (red circles) analysis on images from panel (C).

U87MG tumor-bearing mice by measuring the content of Mn^{2+} using ICP-MS (Figure 3B). High accumulations of Mn^{2+} (15.0 ± 1.4 % ID/g) in tumors was achieved at 12 h post-injection; this showed excellent passive tumor targeting ability (Figure 3B). In the simulated acidic environment (pH 6.5, 1 mM H_2O_2), Mn:CaCO₃-DEX degraded and released Mn^{2+} and exhibited excellent MR imaging ability ($r_1 = 5.8$ mM⁻¹ s⁻¹) (Figure S25A). Positive contrast-enhancement were clearly observed around the injection sites in tumors, when Mn:CaCO₃-DEX was injected directly into tumors of U87MG tumor-bearing mice (Figure S25B, C). Real-time monitoring of the distributions through T₁-weighted MR imaging was important for *in vivo* therapy (Figure 3C). After intravenous injection with Mn:CaCO₃-DEX, T₁-weighted MR imaging of the tumors revealed clear positive-enhancement compared with the pre-injection (Figure 3C). The quantification of the strong positive MR signals in tumors (Figure 3D) proved that the Mn:CaCO₃-DEX could be efficiently accumulated in tumors and gradually reduced to Mn^{2+} , which was finally extracted by renal clearance (red circles in Figure 3C,E). Consistent with the MR imaging results, Mn:CaCO₃-DEX could be obviously observed in the tumor region by Bio-TEM images of tumor tissues (Figure S26).

To detect the generation of $\cdot OH$ in the tumor through the treatment of Mn:CaCO₃-DEX, the tumor-bearing mice were intravenously or intratumoral injected with Mn:CaCO₃-DEX ([Mn]: 2 mg/kg, [DEX]: 4 mg/kg, [Ca]: 5 mg/kg) for fluorescence imaging. The results indicated that Mn:CaCO₃-DEX could produce a large number of $\cdot OH$, inducing cellular oxidative stress (Figure S27).

After confirming the in-situ generation of ions bombs (Ca^{2+} , Mn^{2+} , and HCO_3^-) and release of drug (DEX), The *in vivo* therapeutic effects (enhanced CDT, Ca^{2+} overloading) and anti-inflammatory were evaluated in both subcutaneous and orthotopic tumor models. When the tumor volume reached 60 mm³, the U87MG subcutaneous tumor-bearing mice were randomly divided into 6 groups (n=5) (Figure 4A): (Group 1) PBS; (Group 2) DEX (4 mg/kg, one dose); (Group 3) CaCO₃-DEX ([DEX]: 4 mg/kg, [Ca]: 5 mg/kg, one dose); (Group 4) 2×Mn:CaCO₃-DEX ([Mn]: 4 mg/kg, [DEX]: 8 mg/kg, [Ca]: 10 mg/kg, one dose); (Group 5) Mn:CaCO₃-DEX ([Mn]: 2 mg/kg, [DEX]: 4 mg/kg, [Ca]: 5 mg/kg, four doses); and (Group 6) 2×Mn:CaCO₃-DEX ([Mn]: 4 mg/kg, [DEX]: 8 mg/kg, [Ca]: 10 mg/kg, four doses). The curves in 21-day treatments showed Groups 4-6 had obviously inhibited tumor growth. They had lower tumor weights and smaller tumor sizes compared to Groups 1-3 (Figure 4B, C). We also obtained photographs of

mice in different groups during the treatment to visually assess the effect of treatment (Figure S28). To quantify the treatment effect, the tumor growth inhibition indices (TGIs) were calculated in Equation 1:

$$TGIs = \left[1 - \frac{\text{mean volume of treated tumors}}{\text{mean volume of control tumors}} \right] \times 100\% \quad (1)$$

The TGI values of Group 6 (75.2%) was significantly higher than the low concentration treatment group (Group 5: 57.0%) and low dose treatment group (Group 4: 41.1%). These results proved that there was a close relation between the therapeutic effect and the administration dosage and interval.

To highlight the necessity of nanomaterials in synergistic oncotherapy, the group $MnCl_2 + CaCO_3 + DEX$ ([Mn]: 4 mg/kg, [DEX]: 8 mg/kg, [Ca]: 10 mg/kg, four doses) for tumor therapy was also validated. As shown in Figure S29, the therapeutic effect was not significant.

The hematoxylin & eosin (H&E) staining results of the tumors (Figure 4D) showed significant damage in Group 6 and proved tumor apoptosis and necrosis. The tumor sections were also stained with Alizarin Red S staining, indicating the generation of calcification (Figure 4E). COX-2 expression and the inflammatory cytokine (IL-6) levels in tumors decreased sharply in the successful treatment groups (Figure 4F, G) [72-73]. These results suggest that the superior therapeutic effects in Group 6 were attributed to the combination of anti-inflammatory, cell calcification and HCO₃-enhanced Mn-mediated CDT. Most importantly, during the 21-day therapeutic period, the mice body weight (Figure S30) did not decrease. The H&E staining images of the major organs (Figure S31) after treatments caused no apparent detrimental effects on systemic health, suggesting minimal toxicity to normal cells. Complete serum chemical analysis showed that there were no significant changes after treatment (Figure S32), indicating liver and kidney function of the mice remained normal. After entry into a body, nanoparticles tend to accumulate in liver and lead to hepatic damage, which can be reduced greatly by enhancing Kupffer cell survival. Cytotoxicity *in vitro* proved that Mn:CaCO₃-DEX was nontoxic to Kupffer cell line (Figure S33A). Immunostaining for liver tissues after Mn:CaCO₃-DEX treatment showed Mn:CaCO₃-DEX could not decrease Kupffer cell numbers (Figure S33B-D). These results demonstrated that Mn:CaCO₃-DEX had good biocompatibility, low systemic toxicity and satisfactory tumor suppressive effects.

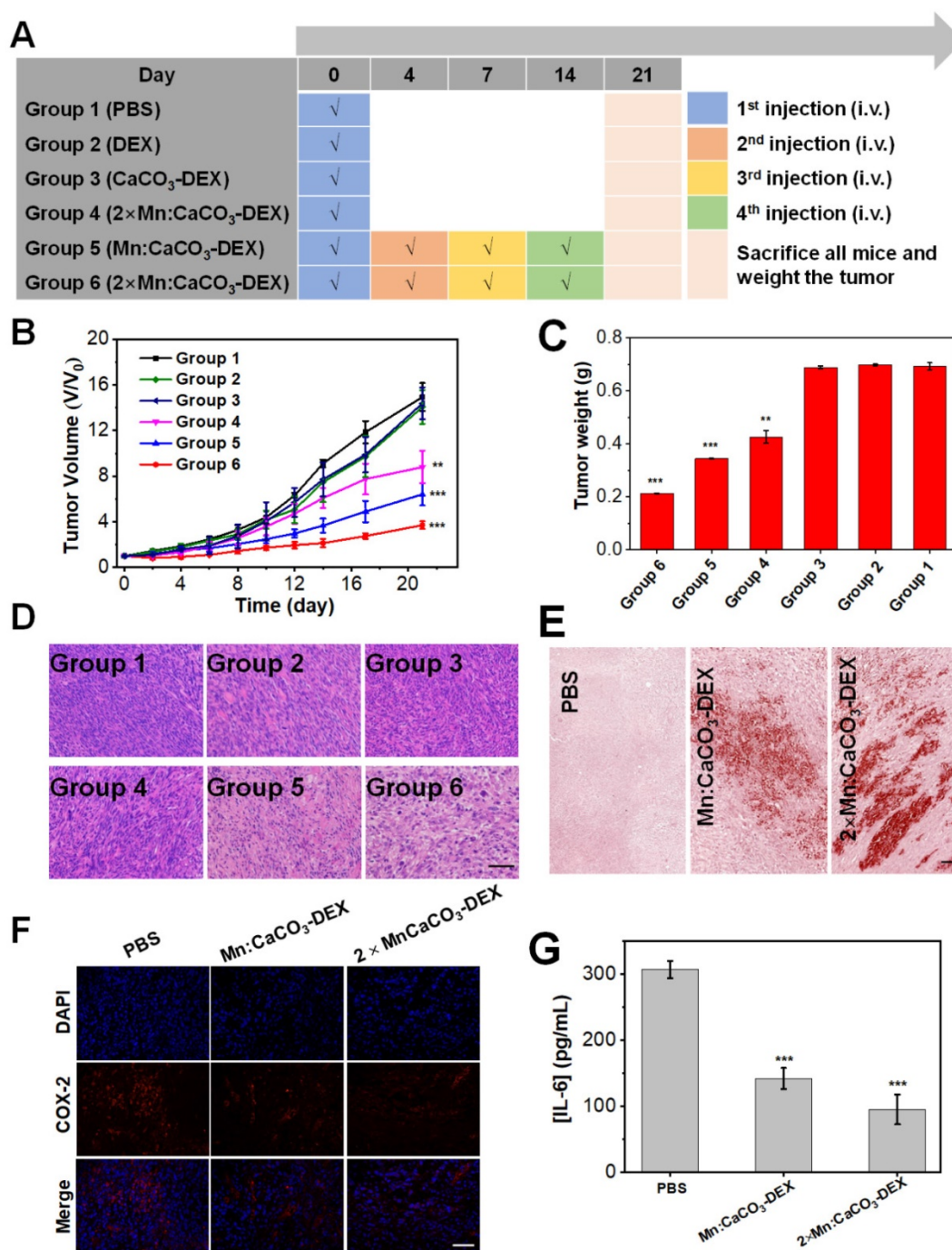


Figure 4. *In vivo* antitumor efficacy for subcutaneous tumor. **(A)** Schematic illustration of the administration design. Groups 1, 2, 3, 4, 5 and 6 were used to represent PBS; DEX (4 mg/kg, one dose); CaCO₃-DEX ([DEX]: 4 mg/kg, [Ca]: 5 mg/kg, one dose); 2×Mn:CaCO₃-DEX ([Mn]: 4 mg/kg, [DEX]: 8 mg/kg, [Ca]: 10 mg/kg, one dose); Mn:CaCO₃-DEX ([Mn]: 2 mg/kg, [DEX]: 4 mg/kg, [Ca]: 5 mg/kg, four doses); 2×Mn:CaCO₃-DEX ([Mn]: 4 mg/kg, [DEX]: 8 mg/kg, [Ca]: 10 mg/kg, four doses). **(B)** Tumor growth curves of U87MG tumor-bearing mice exposed to different formulations after the 21-day treatment period (***p* < 0.01; ****p* < 0.001). **(C)** Final tumor weights of U87MG tumor-bearing mice exposed to different formulations after the 21-day treatment period. **(D)** Hematoxylin & eosin (H&E)-stained tumor sections from U87MG tumor-bearing mice after the 21-day different treatment period (scale bar: 100 μm). **(E)** Alizarin Red S staining of tumor tissue sections from U87MG tumor-bearing mice after the 21-day different treatment period. PBS; Mn:CaCO₃-DEX ([Ca]: 5 mg/kg, four doses); 2×Mn:CaCO₃-DEX ([Ca]: 10 mg/kg, four doses) (scale bar: 100 μm). **(F)** COX-2 immunofluorescence staining of U87MG tumor tissues after the 21-day different treatment period. PBS; Mn:CaCO₃-DEX ([DEX]: 4 mg/kg, four doses); 2×Mn:CaCO₃-DEX ([DEX]: 8 mg/kg, four doses). The blue and red fluorescence indicate cell nucleus and COX-2, respectively (scale bar: 100 μm). **(G)** Secretion levels of pro-inflammatory cytokines (IL-6) in tumors after different treatment. PBS; Mn:CaCO₃-DEX ([DEX]: 4 mg/kg, four doses); 2×Mn:CaCO₃-DEX ([DEX]: 8 mg/kg, four doses). (****p* < 0.001).

We further evaluated the anticancer activity of Mn:CaCO₃-DEX on an orthotopic hepatocellular carcinoma (HepG2). The Alizarin Red S staining results demonstrated the formation of calcification accompanied by the uptake of Mn:CaCO₃-DEX

(Figure 5A). DCFH-DA staining and BODIPY-C11 staining showed significant enhancement of the fluorescence (Figure 5B, C), indicating the efficient generation of ROS and oxidation of lipids. The JC-1 staining results and the release of LDH proved the

dysfunction of mitochondria and breakage of cell membranes (Figures 5D, S34). These dysfunctions resulted in low cell viability after treatment of Mn:CaCO₃-DEX (Figure 5E).

The therapeutic efficiency of Mn:CaCO₃-DEX was further studied on orthotopic liver tumor models. After confirming the establishment of tumors by bioluminescence imaging (BLI), the tumor-bearing mice were divided randomly into 3 groups (n = 5/group): (1) PBS; (2) Mn:CaCO₃-DEX ([Mn]: 2 mg/kg, [DEX]: 4 mg/kg, [Ca]: 5 mg/kg); and (3)

2×Mn:CaCO₃-DEX ([Mn]: 4 mg/kg, [DEX]: 8 mg/kg, [Ca]: 10 mg/kg). Four injections were administrated intravenously on 0, 2, 7 and 14 days. During the treatment, the orthotopic hepatic tumor growth was monitored by BLI every 2 days. The BLI of the injection of Mn:CaCO₃-DEX increased slowly, and the results indicated significant inhibition effects after 24 day of treatment. Versus baseline, a 15.1-fold luminescence enhancement was achieved in PBS group. In contrast, a 8.8-fold enhancement was achieved in the Mn:CaCO₃-DEX group. Significantly,

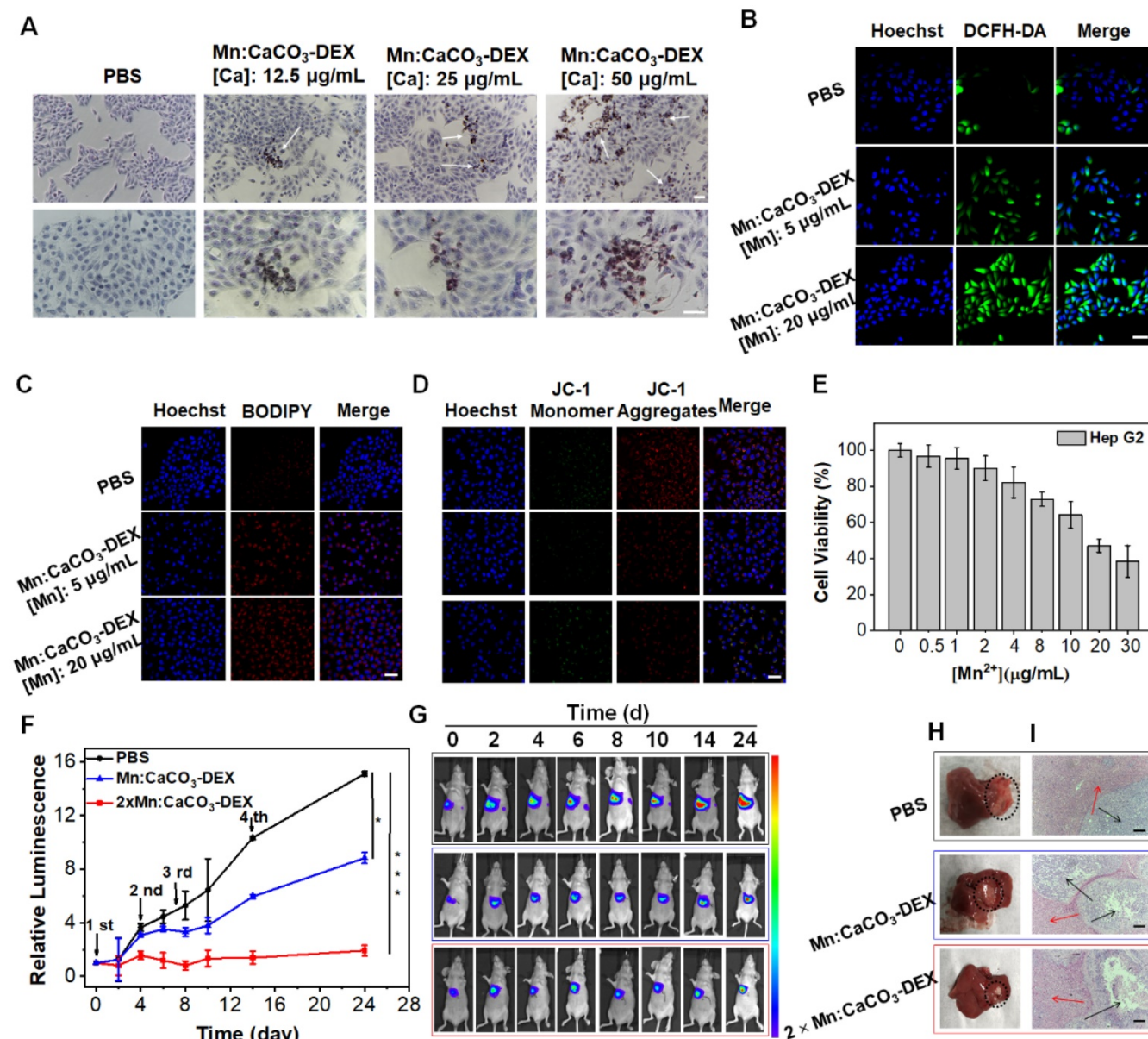


Figure 5. The antitumor efficiency for human hepatocellular carcinoma (HepG2) cells and Orthotopic Hepatic Tumors. (A) Identification of the formation of calcified nodules in HepG2 cells with Alizarin Red S staining, which show the calcified areas in red, respectively (scale bar, 100 µm). **(B)** Intracellular $\cdot\text{OH}$ generation detected by DCFH-DA probe. The blue and green fluorescence indicate cell nucleus and DCFH-DA, respectively (scale bar, 50 µm). **(C)** CLSM observation on the intracellular distribution of lipoperoxides in HepG2 cells after incubation with PBS and different concentration of Mn:CaCO₃-DEX for 24 hours. The red fluorescence is the lipid ROS in cells and membranes after the staining with BODIPY-C11, respectively (scale bar, 50 µm). **(D)** CLSM observation on the changes in the mitochondrial membrane potential of HepG2 cells after incubation with different concentration of Mn:CaCO₃-DEX. The blue, red, and green colors indicate cell nucleus, and JC-1 J-aggregates and monomer, respectively (scale bar, 50 µm). **(E)** Cell viabilities of HepG2 cells incubated with different concentration of Mn:CaCO₃-DEX. **(F)** Relative luminescence intensity changes based on the Bioluminescence images (BLI) (**p* < 0.05; ****p* < 0.001). **(G)** BLI changes of different treatments on days 0–24. **(H)** Photographs of representative tumors taken from orthotopic hepatic tumor-bearing mice after various treatments. **(I)** H&E-stained tumor sections from tumor-bearing mice after various treatments (scale bar: 100 µm).

only a 1.9-fold signal enhancement was seen in the 2×Mn:CaCO₃-DEX group (Figure 5F, G). The photographs of the tumors in excised livers on day 24 clearly showed the size and position of the orthotopic hepatic tumors (Figure 5H, blank circles), confirming the efficient inhibition. More importantly, H&E staining of orthotopic hepatic tumors (Figure 5I, black arrows) showed severely damaged structural disruptions and pathological changes, indicating that high dose of Mn:CaCO₃-DEX caused cancer cell apoptosis. The staining of Alizarin Red S and COX-2 immunohistochemistry again proved the generation of calcification and suppression of inflammation (Figure S35). Furthermore, there was no change in normal liver tissues (Figure 5i, red arrows). The fluctuation of body weight was negligible in all mice (Figure S36). Overall, these results demonstrated that Mn:CaCO₃-DEX had good biocompatibility, and could be an excellent ion drug for precise orthotopic liver cancer therapy.

Conclusion

In summary, a responsive and biodegradable biomaterial—Mn-doped calcium carbonate-dexamethasone phosphate (DEX) nanoparticles (Mn:CaCO₃-DEX)—was reported. Under the acidic environment, Mn:CaCO₃-DEX decomposed to form ions (Mn²⁺, Ca²⁺, CO₃²⁻) and release anti-inflammatory and antitumor drug (DEX). The released ions amplified the oxidative stresses via the *in situ* self-supplying HCO₃⁻-enhanced Mn-mediated CDT. This modulated the tumor environment to inhibit tumor growth. At the same time, the released Ca²⁺ destroyed the intracellular and extracellular ionic gradients to amplify tumor oxidative stress and Ca-overload cell apoptosis and calcification. Furthermore, the released anti-inflammatory drug, DEX, can alleviate the inflammatory environment. The investigations *in vitro* and *in vivo* demonstrated that the synergistic oncotherapy enables synergistic amplification of tumor oxidative stress, reduces inflammation, and induces Ca-overload cell apoptosis to effectively inhibit the growth of subcutaneous tumors. There is almost no influence on normal cells. Overall, Mn:CaCO₃-DEX is an excellent potential agent for precise orthotopic tumor management by simple selecting the coordination pairs between functional organic molecules and metal ions to fit alternate imaging and therapeutic roles.

Supplementary Material

Supplementary methods and figures.

<https://www.thno.org/v12p0734s1.pdf>

Acknowledgements

The work was supported by the National Natural Science Foundation of China (82172007, 81771977, 82001956), the Science Fund for Distinguished Young Scholars of Fujian Province (2021J06007), the National Postdoctoral Program for Innovative Talents (BX20200196), the Xiamen Science and Technology Plan Project (3502Z20183017), the Fundamental Research Funds for the Central Universities of China (20720180054), and the open research fund of National Facility for Translational Medicine (Shanghai) (TMSK-2021-102). All animal experiments were approved by the Animal Management and Ethics Committee of the Xiamen University.

Competing Interests

The authors have declared that no competing interest exists.

References

- Hanahan D, Weinberg RA. Hallmarks of cancer: the next generation. *Cell*. 2011; 144: 646-74.
- Wu Y, Antony S, Meitzler JL, Doroshow JH. Molecular mechanisms underlying chronic inflammation-associated cancers. *Cancer Lett*. 2014; 345: 164-73.
- Coussens LM, Werb Z. Inflammation and cancer. *Nature*. 2002; 420: 860-7.
- DiDonato JA, Mercurio F, Karin M. NF-κB and the link between inflammation and cancer. *Immunol Rev*. 2012; 246: 379-400.
- Hoesel B, Schmid JA. The complexity of NF-κB signaling in inflammation and cancer. *Mol Cancer*. 2013; 12: 86.
- Morris CJ, Earl JR, Trenam CW, Blake DR. Reactive oxygen species and iron—a dangerous partnership in inflammation. *Int J Biochem Cell Biol*. 1995; 27: 109-22.
- Nathan C, Cunningham-Bussell A. Beyond oxidative stress: an immunologist's guide to reactive oxygen species. *Nat Rev Immunol*. 2013; 13: 349-61.
- Volpe CMO, Villar-Delfino PH, dos-Anjos PMF, Nogueira-Machado JA. Cellular death, reactive oxygen species (ROS) and diabetic complications. *Cell Death Dis*. 2018; 9: 119.
- Mi P. Stimuli-responsive nanocarriers for drug delivery, tumor imaging, therapy and theranostics. *Theranostics*. 2020; 10: 4557.
- Chung MF, Chia WT, Wan WL, Lin YJ, Sung HW. Controlled release of an anti-inflammatory drug using an ultrasensitive ROS-responsive gas-generating carrier for localized inflammation inhibition. *J Am Chem Soc*. 2015; 137: 12462-5.
- Jia Z, Wang X, Wei X, Zhao G, Foster KW, Qiu F, et al. Micelle-forming dexamethasone prodrug attenuates nephritis in lupus-prone mice without apparent glucocorticoid side effects. *ACS Nano*. 2018; 12: 7663-81.
- Benedetti S, Pirola B, Poliani PL, Cajola L, Pollo B, Bagnati R, et al. Dexamethasone inhibits the anti-tumor effect of interleukin 4 on rat experimental gliomas. *Gene Ther*. 2003; 10: 188-92.
- Ozbakir B, Crielaard BJ, Metselaar JM, Storm G, Lammers T. Liposomal corticosteroids for the treatment of inflammatory disorders and cancer. *J Controlled Release*. 2014; 190: 624-36.
- Yoshimura K, Minami T, Nozawa M, Kimura T, Egawa S, Fujimoto H, et al. A phase 2 randomized controlled trial of personalized peptide vaccine immunotherapy with low-dose dexamethasone versus dexamethasone alone in chemotherapy-naive castration-resistant prostate cancer. *Eur Urol*. 2016; 70: 35-41.
- Ma R, Zhang W, Tang K, Zhang H, Zhang Y, Li D, et al. Switch of glycolysis to gluconeogenesis by dexamethasone for treatment of hepatocarcinoma. *Nat Commun*. 2013; 4: 2508.
- Coimbra M, Rijcken CJF, Stigter M, Hennink WE, Storm G, Schiffelers RM. Antitumor efficacy of dexamethasone-loaded core-crosslinked polymeric micelles. *J Controlled Release*. 2012; 163: 361-7.

17. Wang H, Wang Y, Rayburn ER, Hill DL, Rinehart JJ, Zhang R. Dexamethasone as a chemosensitizer for breast cancer chemotherapy: potentiation of the antitumor activity of adriamycin, modulation of cytokine expression, and pharmacokinetics. *Int J Clin Oncol*. 2007; 30: 947-53.
18. Clapham DE. Calcium signaling. *Cell*. 1995; 80: 259-68.
19. Yu SP, Canzoniero LM, Choi DW. Ion homeostasis and apoptosis. *Curr Opin Cell Biol*. 2011; 13: 405-11.
20. Carafoli E, Brini M. Calcium signalling and disease. *Subcell Biochem*. 2007; 45: 1-566.
21. Felsenfeld A, Rodriguez M, Levine B. New insights in regulation of calcium homeostasis. *Curr Opin Nephrol Hypertens*. 2013; 22: 371-6.
22. Orrenius S, Zhivotovsky B, Nicotera P. Regulation of cell death: the calcium-apoptosis link. *Nat Rev Mol Cell Biol*. 2003; 4: 552-65.
23. Monteith GR, Davis FM, Roberts-Thomson SJ. Calcium channels and pumps in cancer: changes and consequences. *J Biol Chem*. 2012; 287: 31666-73.
24. Dong Z, Feng L, Hao Y, Li Q, Chen M, Yang Z, et al. Synthesis of CaCO₃-based nanomedicine for enhanced sonodynamic therapy via amplification of tumor oxidative stress. *Chem*. 2020; 6: 1391-407.
25. Zhang M, Song R, Liu Y, Yi Z, Meng X, Zhang J, et al. Calcium-overload-mediated tumor therapy by calcium peroxide nanoparticles. *Chem*. 2019; 5: 2171-82.
26. Orrenius S, Gogvadze V, Zhivotovsky B. Calcium and mitochondria in the regulation of cell death. *Biochem Biophys Res Commun*. 2015; 460: 72-81.
27. Kumar S, Kain V, Sitasawad SL. High glucose-induced Ca²⁺ overload and oxidative stress contribute to apoptosis of cardiac cells through mitochondrial dependent and independent pathways. *Biochim Biophys Acta*. 2012; 1820: 907-20.
28. Lin LS, Wang JW, Song J, Liu Y, Zhu G, Dai Y, et al. Cooperation of endogenous and exogenous reactive oxygen species induced by zinc peroxide nanoparticles to enhance oxidative stress-based cancer therapy. *Theranostics*. 2019; 9: 7200.
29. Floersheim GL. Calcium antagonists protect mice against lethal doses of ionizing radiation. *Br J Radiol* 1992; 65: 1025-9.
30. Elmslie KS. Calcium channel blockers in the treatment of disease. *J Neurosci Res*. 2004; 75: 733-41.
31. Brini M, Carafoli E. Calcium pumps in health and disease. *Physiol Rev*. 2009; 89: 1341-78.
32. Penner R, Matthews G, Neher E. Regulation of calcium influx by second messengers in rat mast cells. *Nature*. 1988; 334: 499-504.
33. Xue CC, Li MH, Zhao Y, Zhou J, Hu Y, Cai KY, et al. Tumor microenvironment-activatable Fe-doxorubicin preloaded amorphous CaCO₃ nanoformulation triggers ferroptosis in target tumor cells. *Sci Adv*. 2020; 6: eaax1346.
34. Wan X, Zhong H, Pan W, Li Y, Chen Y, Li N, et al. Programmed release of dihydroartemisinin for synergistic cancer therapy using a CaCO₃ mineralized metal-organic framework. *Angew Chem, Int Ed Engl*. 2019; 58: 14134-9.
35. Dong Z, Feng L, Hao Y, Chen M, Gao M, Chao Y, et al. Synthesis of hollow biomineralized CaCO₃-polydopamine nanoparticles for multimodal imaging-guided cancer photodynamic therapy with reduced skin photosensitivity. *J Am Chem Soc*. 2018; 140: 2165-78.
36. Huang LL, Li X, Zhang J, Zhao QR, Zhang MJ, Liu AA, et al. MnCaS-biomineralized oncolytic virus for bimodal imaging-guided and synergistically enhanced anticancer therapy. *Nano Lett*. 2019; 19: 8002-9.
37. Zhao Y, Luo Z, Li M, Qu Q, Ma X, Yu SH, et al. A preloaded amorphous calcium carbonate/doxorubicin@silica nanoreactor for pH-responsive delivery of an anticancer drug. *Angew Chem, Int Ed Engl*. 2015; 54: 919-22.
38. Zhang L, Wan SS, Li CX, Xu L, Cheng H, Zhang XZ. An adenosine triphosphate-responsive autocatalytic Fenton nanoparticle for tumor ablation with self-supplied H₂O₂ and acceleration of Fe(III)/Fe(II) conversion. *Nano Lett*. 2018; 18: 7609-18.
39. Tang Z, Liu Y, He M, Bu W. Chemodynamic therapy: tumour microenvironment-mediated Fenton and Fenton-like reactions. *Angew Chem, Int Ed Engl*. 2019; 58: 946-56.
40. Lin LS, Song J, Song L, Ke K, Liu Y, Zhou Z, et al. Simultaneous Fenton-like ion delivery and glutathione depletion by MnO₂-based nanoagent to enhance chemodynamic therapy. *Angew Chem, Int Ed Engl*. 2018; 57: 4902-6.
41. Zhong X, Wang X, Cheng L, Tang Y, Zhan G, Gong F, et al. GSH-depleted PtCu₃ nanocages for chemodynamic-enhanced sonodynamic cancer therapy. *Adv Funct Mater*. 2019; 30: 1907954.
42. Stohs SJ, Bagchi D. Oxidative mechanisms in the toxicity of metal ions. *Free Radical Biol Med*. 1995; 18: 321-36.
43. Poeggeler B, Reiter RJ, Tan DX, Chen LD, Manchester LC. Melatonin, hydroxyl radical-mediated oxidative damage, and aging: a hypothesis. *J Pineal Res*. 1993; 14: 151-68.
44. He T, Qin X, Jiang C, Jiang D, Lei S, Lin J, et al. Tumor pH-responsive metastable-phase manganese sulfide nanotheranostics for traceable hydrogen sulfide gas therapy primed chemodynamic therapy. *Theranostics*. 2020; 10: 2453.
45. Schieber M, Chandel NS. ROS function in redox signaling and oxidative stress. *Curr Biol*. 2014; 24: R453-R62.
46. Gorrini C, Harris IS, Mak TW. Modulation of oxidative stress as an anticancer strategy. *Nat Rev Drug Discovery*. 2013; 12: 931-47.
47. Riley PA. Free radicals in biology : oxidative stress and the effects of ionizing radiation. *Int J Radiat Biol*. 1994; 65 38-44.
48. Ercal N, Gurer-Orhan H, Aykin-Burns N. Toxic metals and oxidative stress part I: mechanisms involved in metal-induced oxidative damage. *Curr Top Med Chem*. 2001; 1: 529-39.
49. Imlay JA, Chin SM, Linn S. Toxic DNA damage by hydrogen peroxide through the Fenton reaction in vivo and in vitro. *Science* 1988; 240: 640-2.
50. Imlay JA, Linn S. DNA damage and oxygen radical toxicity. *Science*. 1988; 240: 1302-9.
51. Sang M, Luo R, Bai Y, Dou J, Zhang Z, Liu F, et al. Mitochondrial membrane anchored photosensitive nano-device for lipid hydroperoxides burst and inducing ferroptosis to surmount therapy-resistant cancer. *Theranostics*. 2019; 9: 6209.
52. Bartolozzi C, Donati F, Cioni D, Crocetti L, Lencioni R. MnDPDP-enhanced MRI vs dual-phase spiral CT in the detection of hepatocellular carcinoma in cirrhosis. *Eur Radiol*. 2000; 10: 1697-702.
53. Thomsen HS, Barentsz JO, Burcharth F, Chabanova E, Dekker HM, Moesgaard F, et al. Initial clinical experience with oral manganese (CMC-001) for liver MR imaging. *Eur Radiol*. 2007; 17: 273-8.
54. Ding B, Zheng P, Jiang F, Zhao Y, Wang M, Chang M, et al. MnO_x nanospikes as nanoadjuvants and immunogenic cell death drugs with enhanced antitumor immunity and antimetastatic effect. *Angew Chem, Int Ed Engl*. 2020; 59: 16381-4.
55. Lin X, Liu S, Zhang X, Zhu R, Chen S, Chen X, et al. An ultrasound activated vesicle of janus Au-MnO nanoparticles for promoted tumor penetration and sono-chemodynamic therapy of orthotopic liver cancer. *Angew Chem, Int Ed Engl*. 2020; 59: 1682-8.
56. Fu LH, Hu YR, Qi C, He T, Jiang S, Jiang C, et al. Biodegradable Manganese-doped Calcium phosphate nanotheranostics for traceable cascade reaction-enhanced anti-tumor therapy. *ACS Nano*. 2019; 13: 13985-94.
57. Ember E, Rothbart S, Puchta R, Eldik Rv. Metal ion-catalyzed oxidative degradation of Orange II by H₂O₂: High catalytic activity of simple manganese salts. *New J Chem*. 2009; 33: 34-49.
58. Meng ZH, Wu SH, Sun SW, Xu Z, Zhang XC, Wang XM, et al. Formation and oxidation reactivity of MnO₂⁺(HCO₃)_n in the Mn^{II}(HCO₃)-H₂O₂ System. *Inorg Chem*. 2020; 59: 3171-80.
59. Wang P, Liang C, Zhu J, Yang N, Jiao A, Wang W, et al. Manganese-based nanoplatform as metal ion-enhanced ROS generator for combined chemodynamic/photodynamic therapy. *ACS Appl Mater Interfaces*. 2019; 11: 41140-7.
60. Miao Z, Huang D, Wang Y, Li W, Fan L, Wang J, et al. Safe-by-design exfoliation of niobium diselenide atomic crystals as a theory-oriented 2D nanoagent from anti-inflammation to antitumor. *Adv Funct Mater*. 2020; 30: 2001593.
61. Yao Y, Yao QY, Xue JS, Tian XY, An QM, Cui LX, et al. Dexamethasone inhibits pancreatic tumor growth in preclinical models: Involvement of activating glucocorticoid receptor. *Toxicol Appl Pharmacol*. 2020; 401: 115118.
62. Liochev SI, Fridovich I. Carbon dioxide mediates Mn(II)-catalyzed decomposition of hydrogen peroxide and peroxidation reactions. *Proc Natl Acad Sci U S A*. 2004; 101: 12485-90.
63. Gregory CA, Gunn WG, Peister A, Prockop DJ. An Alizarin red-based assay of mineralization by adherent cells in culture: comparison with calcein/strontium chloride extraction. *Anal Biochem*. 2004; 329: 77-84.
64. Davis JT. Ion transport: tipping a cell's ionic balance. *Nat Chem*. 2014; 6: 852-3.
65. Bucci M, Finkelstein JM, Goodman C, Miura G, Sheppard TL. Death by ions. *Nat Chem Biol*. 2014; 10: 795-.
66. Buschaert N, Park SH, Baek KH, Choi YP, Park J, Howe ENW, et al. A synthetic ion transporter that disrupts autophagy and induces apoptosis by perturbing cellular chloride concentrations. *Nat Chem*. 2017; 9: 667-75.
67. Saha R, Saha N, Donofrio RS, Bestervelt LL. Microbial siderophores: a mini review. *J Basic Microbiol*. 2013; 53: 303-17.
68. Ballouche M, Cornelis P, Baysse C. Iron metabolism: a promising target for antibacterial strategies. *Recent Pat Anti-Infect Drug Discovery*. 2009; 4: 190-205.

69. Ko SK, Kim SK, Share A, Lynch VM, Park J, Namkung W, et al. Synthetic ion transporters can induce apoptosis by facilitating chloride anion transport into cells. *Nat Chem*. 2014; 6: 885-92.
70. Glitsch MD, Bakowski D, B.Parekh A. Store-operated Ca^{2+} entry depends on mitochondrial Ca^{2+} uptake. *EMBO J*. 2002; 21: 6744-54.
71. Yang Y, Guo L, Wang Z, Liu P, Liu X, Ding J, et al. Targeted silver nanoparticles for rheumatoid arthritis therapy via macrophage apoptosis and Re-polarization. *Biomaterials*. 2021; 264: 120390.
72. Liang H, Peng B, Dong C, Liu L, Mao J, Wei S, et al. Cationic nanoparticle as an inhibitor of cell-free DNA-induced inflammation. *Nat Commun*. 2018; 9: 4291.
73. Ma S, Song W, Xu Y, Si X, Zhang D, Lv S, et al. Neutralizing tumor-promoting inflammation with polypeptide-dexamethasone conjugate for microenvironment modulation and colorectal cancer therapy. *Biomaterials*. 2020; 232: 119676.